Additive Manufacturing 31 (2020) 100929

Contents lists available at ScienceDirect

Additive Manufacturing

journal homepage: www.elsevier.com/locate/addma

Full Length Article

Influence of particle morphology and size distribution on the powder flowability and laser powder bed fusion manufacturability of Ti-6Al-4V alloy

Salah Eddine Brika[a], Morgan Letenneur[a], Christopher Alex Dion[b], Vladimir Brailovski[a,*]

[a] Department of Mechanical Engineering, École de technologie supérieure, 1100 Notre-Dame Street West, Montreal, QC H3C 1K3, Canada
[b] Research and Development, PyroGenesis Additive, 1744, William St., Suite 200, Montréal, QC H3J 1R4, Canada

ARTICLE INFO

Keywords:
Laser powder bed fusion
Particle size distribution
Sphericity
Ti-6Al-4V
Layer thickness
Powder flowability

ABSTRACT

Laser powder bed fusion (LPBF) additive manufacturing technology is sensitive to variations in powder particle morphology and size distribution. However, the absence of a clear link between the powder characteristics and the LPBF performances complicates the development, selection and quality control of LPBF powder feedstock. In this work, three Ti-6Al-4 V powder lots produced by two different techniques, namely, plasma atomization and gas atomization, were selected and characterized. Following the micro-computed tomography analysis of the powder particles' morphology, size and density, the flowability of these powder lots was concurrently evaluated using Hall and Gustavsson flowmeters and an FT4 powder rheometer. Using established rheology-based criteria, a figure of merit was proposed to quantify the overall powder suitability for the LPBF process. Next, the same three powder lots were used to 3D-print and post-process a series of testing specimens with different layer thicknesses and build orientations, in order to establish a correlation between the powder characteristics and the geometric and mechanical properties of a final product. This study demonstrates that the use of highly spherical powders with a limited amount of fine particles promotes their flowability and yields LPBF components with improved mechanical and geometric characteristics.

1. Introduction

Laser powder bed fusion (LPBF) is a rapidly expanding technology for the additive manufacturing of complex metallic parts. The technology works by stacking successive layers of fused metal powder to form a part [1]. With the LPBF process, each layer of the part is created using a high power laser that selectively fuses particles laying on the powder bed; then, a recoating system uniformly spreads a new layer of powder over the previously fused one – to create a next layer and so on, until the entire part is formed [2].

A large variety of metals and metallic alloys can be employed to manufacture parts using the LPBF process. The powder feedstock is generally obtained using the gas or plasma atomization techniques. Some recent studies have also shown the relevance of water-atomized powders for AM applications [3,4]. As discussed in [5,6], each production technique is known to yield a certain set of specific powder characteristics in terms of morphology, size, porosity, and chemical composition of powder particles.

The above-mentioned characteristics are the main factors influencing the rheological behavior and packing efficiency of the powder, and represents an area of research interest, which has led to numerous studies investigating this relationship [7–9]. In the context of these studies, several relations between the powders' characteristics and their rheological behavior have been established, for example: a wider particle size distribution (PSD) increases the packing density, but decreases the powder flowability; coarse particles have better flowability than their fine counterparts; spherical particles simultaneously promote both the powder packing efficiency and the powder flowability, etc.

A number of studies investigating the influence of certain powder characteristics on the mechanical properties of printed parts can also be reported. A large part of these publications focuses on the impact of particle size distributions. For example, Spierings and Herres [10] showed that when a PSD of 316 L stainless steel powder is shifted towards fine particles, powder packing, and therefore printed part density and surface finish are improved. On the other hand, when this PSD is shifted towards coarse particles, higher elongations at break are obtained. Comparable results were published in [8,11,12].

Next, Liu and Wildman [13] studied gas-atomized 316 L stainless steel powders and reported that the narrower the particle size distribution, the higher the mechanical resistance and hardness of printed

* Corresponding author.
E-mail addresses: salah-eddine.brika.1@etsmtl.net (S.E. Brika), morgan.letenneur.1@etsmtl.net (M. Letenneur), cdion@pyrogenesis.com (C.A. Dion), vladimir.brailovski@etsmtl.ca (V. Brailovski).

https://doi.org/10.1016/j.addma.2019.100929
Received 6 August 2019; Received in revised form 28 October 2019; Accepted 28 October 2019
Available online 06 November 2019

Nomenclature

AB	As built
AE	Aeration energy
AM	Additive manufacturing
AMS	AM suitability factors
BFE	Basic flow energy
BR	Build rate
CI	Compressibility index
D_v	Diameter of a volume-equivalent sphere
E	Energy density
E	Young's modulus
h	Hatch spacing
HSS	High speed steel
LPBF	Laser powder bed fusion
m_{air}	Sample's mass in the air
m_{water}	Sample's mass in the water
NMP	Average normalized mechanical performance
P	Laser power
PBD	Powder bed density
PD	Pressure drop
PSD	Particle size distribution
R_a	Profile roughness arithmetical mean
SE	Specific energy
SEM	Scanning electron microscope
Sp	Surface area of a particle of a given volume
SR	Stress relief
Ss	Surface area of an equivalent sphere with the same volume as the particle studied
UTS	Ultimate tensile strength
YS	Tensile strength
t	Layer thickness
v	Scan speed
V_p	Volume of the particle
XY	Horizontal build direction
Z	Vertical build direction
δ	Elongation at break
μ-CT	Micro computed tomography
ρ_c	Conditioned bulk density
c	Cohesion coefficient
ρ_{water}	Water density

components. The authors also evaluated powder bed densities by designing a special container trapping powder during the build, and demonstrated a direct correlation between the measured powder bed density and the density of printed parts. More counterintuitive results were found in [14] where AlSi10Mg powder with a wider powder size distribution resulted in a more efficient powder packing, but relatively modest printed part densities. Furthermore, Seyda and Herzog [5] compared three Ti-6Al-4 V powders from different production routes. Despite differences in terms of particles morphology, surface roughness and powder size distribution, comparable results in terms of part densities and mechanical properties were reported. On the other hand, however, Baitimerov and Lykov [15] studied three different AlSi12 powder batches and reported that a batch with better followability and packing density yielded printed parts with higher densities.

Notable discrepancies in the results obtained indicate that the relationship between the characteristics of powder feedstock and those of printed parts is complex and depends not only on the powder chemistry, particle morphology and size distribution but also on the performances of a given LPBF system. From this assertion stems the necessity to adapt the existing powder characterization techniques to the LPBF process, and to propose novel experimental procedures and numerical tools allowing the prediction of the in-process performances of powder feedstocks, as clearly expressed in [16–18].

In this work, to continue bridging the aforementioned gap, a comparative study of three Ti-6Al-4V powder lots is carried out using different powder characterization techniques. The study starts with the geometric characterization of different powder lots (PSD, morphology, porosity), continues with their flowability study, and ends with the mechanical and geometric characterization of components printed with these powder lots.

2. Methodology

For the present study, the following workflow was established:

- Select powder lots to study
- Carry out geometric and rheological analyses of the selected powders
- Print specimens from the selected powders and characterize their powder bed and printed densities, geometric attributes, and mechanical properties

2.1. Selection of powder lots

To assess the impact of powders' PSD, morphology and porosity on their flowability and LPBF process performances (surface finish and accuracy, smallest printable features, and mechanical properties), three Ti-6Al-4V powder lots were ordered from two suppliers employing two different production techniques, namely gas atomization and plasma atomization; the latter is known to yield more spherical and less porous powders as compared to the former [5,6].

For this study, three powder lots were selected, namely:

- Powder 1 from gas atomization production route.
- Powder 2 from plasma atomization production route with a PSD close to that of Powder 1.
- Powder 3 from plasma atomization production route with a PSD slightly different from those of Powders 1 and 2.

Powder 1 was supplied by EOS (EOS GmbH, Munich, Germany). Powders 2 and 3 were supplied by PyroGenesis (PyroGenesis Additive, Montreal, Canada): Powder 2 corresponds to a standard 20–53 μm product, while Powder 3 corresponds to a 15–45 μm.

The comparison between Powders 1 and 2 is expected to allow clarifying the impact of sphericity and porosity of powder particles on the LPBF process performances, while the comparison between Powders 2 and 3 is expected to provide an insight into how the LPBF process performances are affected by variations in powders' PSDs.

Chemical compositions of three powder lots were provided by the powders producers and all of them respect the specifications defined by the ASTM B348 – grade 23 Standard as shown in Table 1.

Table 1
Chemical compositions of three powder lots studied in this work (in wt. %).

Element	Powder 1	Powder 2	Powder 3	ASTM B348	Test method
C	0.01	0.01	0.02	0.08 (max)	ASTM E1941
O	0.11	0.12	0.11	0.13 (max)	ASTM E1409
N	0.020	0.004	0.020	0.030 (max)	ASTM E1409
H	0.0030	0.0037	0.0080	0.01250 (max)	ASTM E1447
Fe	0.190	0.145	0.180	0.250 (max)	ASTM E2371
Al	6.30	6.21	6.26	5.50-6.50 (range)	ASTM E2371
V	4.10	4.00	3.85	3.50-4.50 (range)	ASTM E2371
Ti	Balance	Balance	Balance	Balance	ASTM E2371

2.2. Powder lots characterization

2.2.1. Particle size distribution, morphology and porosity

Powder particles were analyzed using an XT H225 X-ray μ-CT (computed tomography) system (Nikon, MI, USA). A plastic capillary tube (inner diameter of 0.8 mm, wall thickness of 0.1 mm, length of 32 mm) was filled with powder, sealed and installed on a μ-CT sample holder. The samples were scanned using a transmission scan source with a Beryllium target configured with a 145 kV scan voltage and 19 μA beam current. The scanned volume was then reconstructed using the CT Pro 3D software (Nikon, MI, USA) with a voxel size of 1.331 μm^3. The file obtained was analyzed using the Dragonfly software (Object Research Systems, QC, Canada) allowing the isolation of powder particles, the generation of their 3D representations and the calculation of several metrics of interest for each of them. First, Dragonfly was used for pore detection in powder particles and the evaluation of their cumulative volumes. Next, the particles sphericity was estimated using the following formula [19]:

$$Sphericity = \frac{Ss}{Sp} \tag{1}$$

where Sp is the surface area of a particle of a given volume and Ss, the surface area of an equivalent sphere with the same volume as the particle studied. Particles' morphology was also analyzed visually by a Hitachi TM3000 scanning electron microscope (Tokyo, Japan).

Finally, the volume-based particle size distributions were generated by evaluating the diameters of volume-equivalent spheres using the following formula [19]:

$$D_v = \left(\frac{6}{\pi} V_p\right)^{1/3} \tag{2}$$

where D_v is the diameter of a volume-equivalent sphere and V_p, the volume of the particle.

2.2.2. Rheological properties

The flowability of powders was evaluated using three characterization setups: Hall and Gustavsson flowmeters and an FT4 powder rheometer (Freeman Technology, UK). Hall and Gustavsson flowmeters are common measurement setups used in the industry to assess metal powder flow rates. The main differences between them is that the funnel angle in the Gustavsson flowmeter is steeper, while the bottom opening is smaller as compared to the Hall flowmeter, thus making the former more adapted for poor flowing powders. Both methods were employed in this work to facilitate the comparison with other ASTM/ISO-based studies. ASTM-B213 2017 standard was used for the Hall flowmeter measurements and ISO-13517 was followed for the Gustavsson flowmeter measurements.

An FT4 powder rheometer, being more sensitive than the rather simplistic funnel-based techniques, is intended to provide a finer evaluation of the rheological behavior of powders. Several testing modes are available for evaluating the powder behavior under various conditions, with each mode providing some insights into the powder rheology. Detailed presentation of the available testing modes and a complete list of software outputs of FT4 powder rheometers can be found in the manufacturer's documentation and publications [20,21]. For this study, five testing modes were selected, namely dynamic flow, aeration, permeability, compressibility, and shear testing modes. The following is a brief presentation of these testing modes.

1 In the dynamic flow test, a vessel is filled with powder and the torque applied by the rotating blade moving through the powder bed is recorded. The program output includes several metrics: the basic flow energy (BFE), which represents the energy recorded in the seventh repetition during the downward motion (confined motion), the conditioned bulk density (ρ_c), which represents a bulk density of the conditioned powder bed, and the specific energy (SE), which represents the energy recorded during the upward traverse of the blade (unconfined motion).
2 The FT4 powder aeration test allows the measurement of the flow energy of a loosely packed powder bed by introducing air at different velocities and recording the resistance to the blade rotation. The software outputs include the aeration energy (AE).
3 Powder compressibility is evaluated by applying an increasing compressive load with a vented piston to evaluate the powder bed volume change as a function of the applied force. A compressibility index (CI) is generated by dividing the compressed powder bed density by the conditioned bulk density (ρ_c) measured prior to start of the compression cycle.
4 The FT4 permeability test measures the ease with which a powder bed releases entrapped air. Air is introduced at the bottom of the powder column and increasing levels of compressive force are applied with a vented piston. During the test, the air pressure is monitored as a function of the applied load, and the pressure drop (PD) is calculated.
5 The FT4 powder rheometer allows also the evaluation of shear stresses required to initiate the powder flow under consolidation. As an output, several metrics of interest can be extracted, one of them being the cohesion coefficient (c).

For each rheological assessment mode presented above, the measurements were replicated three times using fresh samples of each powder, and the average and standard deviation values were calculated.

Note that flowability is not an inherent property of powder, but rather, it is a function of the ability of powder to flow in a desired manner in a given application. A review of the LPBF literature indicates the benefits of maximizing the powder bed density in order to minimize the by-products porosity, improve heat dissipation and powder absorptivity, in addition to homogenize the interactions between the laser beam and the newly deposited powder layer (interaction laser-gas voids differs from interaction laser-material) [22–26]. Powder bed uniformity is also an influential factor on the quality of LPBF builds where uneven layers (thickness, curliness, agglomerates) may lead to variations in the dynamics of the laser-material interactions, thus causing some processing issues [27,28]. The goal during the recoating operation of the LPBF process is to spread a thin, dense and uniform powder layer, while causing minimum disturbances to the parts being manufactured and to the loosen powder surrounding the printed part. In order to facilitate the comparison of three powder lots and evaluate their suitability for LPBF, different criteria were defined and expressed in terms of the FT4 generated indices as shown in Table 2.

Table 2
Rheology-based criteria for the LPBF suitability of metallic powders (up ↑ and down ↓ arrow directions indicate the favorable trends for LPBF).

	Criterion	FT4 indices
Powder bed density	Good packing ability	↑Conditioned bulk density (ρ_c) ↓Compressibility (CI)
	Low entrapped air	↑Conditioned bulk density (ρ_c) ↓Compressibility (CI)
	Good ability to release entrapped air	↑Permeability (↓PD)
Powder bed uniformity	Low tendency to agglomerate	↓Aeration energy (AE)
	Low mechanical interlocking	↓Specific energy (SE) ↓Cohesion coefficient (c)
Minimal disturbances	Low resistance to flow	↓Specific energy (SE) ↓Basic flow energy (BFE)

↑: index to maximize, ↓: index to minimize.

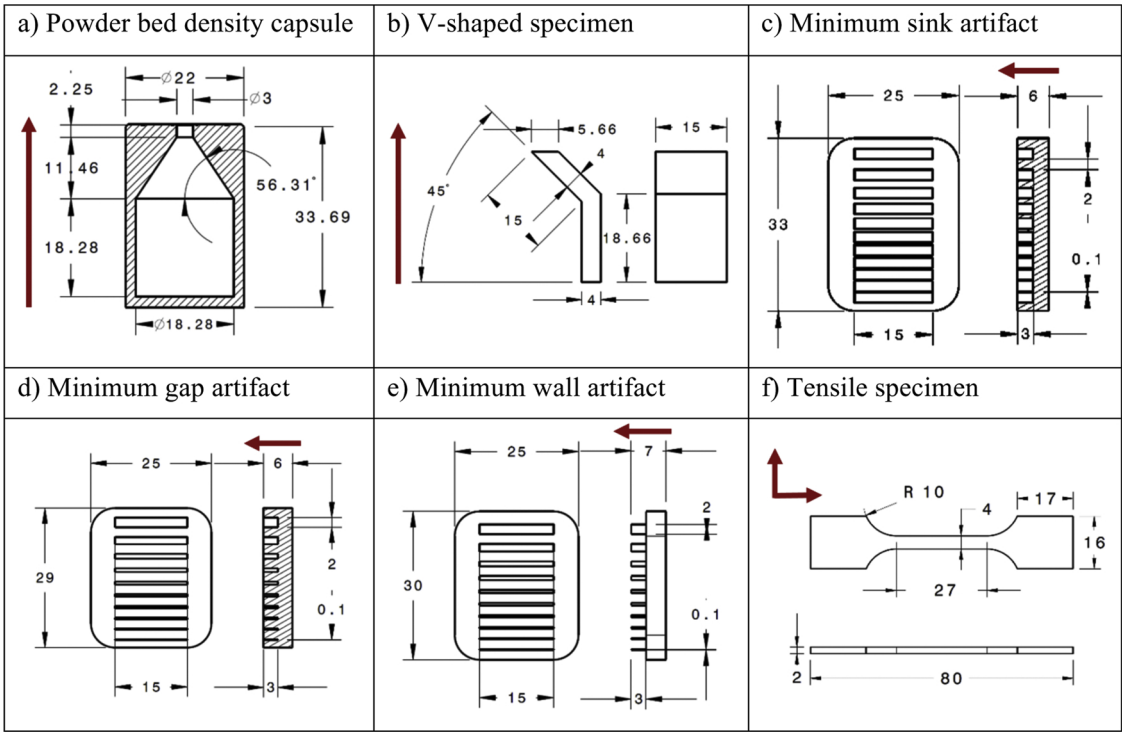

Fig. 1. Printed specimens (dimensions in mm): a) powder bed density capsule, b) V-shaped specimen, c) minimum sink artifact, d) minimum gap artifact, e) minimum wall artifact, f) tensile specimen machined from blanks (printed in horizontal and vertical directions); bold arrows indicate the build orientation of each specimen.

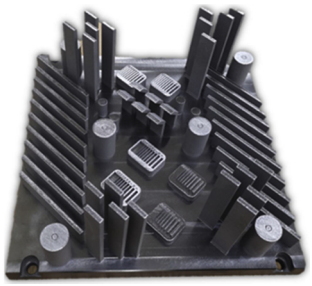

Fig. 2. Example of a build plate with printed specimens for process characterization.

2.3. LPBF specimens manufacture

Various characterization specimens were manufactured with the selected powder lots to link the particles' morphology and size distribution to the LPBF process performances, more specifically the powder bed and printed part densities, as well as to the surface finish, accuracy, minimum printable design features and mechanical properties of printed parts. The following is the list of the specimens manufactured (see also Figs. 1 and 2):

- Powder bed density specimens (Fig. 1a adapted from [26])
- Printed part density specimens (8 mm-diameter, 15 mm-height cylindrical samples); not shown
- V-shaped roughness specimens containing four planar faces oriented to the build plate under angles 0, 45, 90 and 135° ((Fig. 1b) adapted from [29])
- Geometric artifacts: sink, gap and wall minimum printable design features in the range of 0.1 to 2 mm: (Fig. 1c-d-e) adapted from [30]
- Tensile specimens (Fig. 1f) with two build orientations; "XY" (horizontal - along the build plate) and "Z" (vertical - perpendicular to the build plate), in conformity with ASTM–E8/E8M 2016 specifications

All the specimens of this study were manufactured with two powder layer thicknesses (30 and 60 µm) using an M280 400 W Ytterbium fiber laser system (EOS GmbH, Munich, Germany) equipped with a HSS (high speed steel) doctor blade and the default programs provided by the manufacturer for these two layer thicknesses, namely, the "Ti64 Performance", for a 30 µm layer thickness and the "Ti64 Speed", for a 60 µm layer thickness (PSW version 3.6). The respective LPBF parameter sets are listed in Table 3.

The energy density (E, J/mm^3) and the build rate (BR, cm^3/h) are defined by Eqs. (3) and (4):

$$E\ (J/mm^3) = \frac{P}{h*v*t} \tag{3}$$

$$BR\ (cm^3/h) = h*v*t \tag{4}$$

where P is the laser power; h, the hatching space; v, the scanning speed, and t, the layer thickness.

Several replicates (6 powder bed density capsules, 2 printed density specimens, 3 V-shaped surface roughness specimens, 2 geometric artifacts and 5 prismatic blanks for tensile specimens) were printed for each type of specimens. The specimens' positions were kept identical during repetitive builds (two for each powder lot). All powder bed density specimens (Fig. 1a) and some prismatic blanks were reserved in the as-built state, while the remaining specimens were heat-treated using the EOS-recommended stress relief conditions (800 °C for 4 h in argon atmosphere) and a Nabertherm N41/H furnace (Lilienthal, Germany). The specimens were detached from the build plate using a band saw.

Note that rectangular prismatic 80 × 16 × 3 mm^3 blanks produced in two build orientations were machined to obtain dumbbell-shaped tensile specimens with a gauge length of 27 mm according to the ASTM-

Table 3
Printing parameters.

Power (W)	Speed (mm/s)	Hatching (mm)	Layer thickness (mm)	Build rate (cm^3/h)	Energy density (J/mm^3)
280	1200	0.14	0.03	18.1	27.8
340	1250	0.12	0.06	32.4	37.8

E8/E8M 2016 standard specifications as shown in Fig. 1f. The effect of the build orientation (vertical or horizontal), the post-processing treatment (as-built "AB" and stress-relieved "SR"), and the layer thickness (30 and 60 μm) were investigated.

2.4. Measurements of powder bed density and characterization of printed specimens

2.4.1. Powder bed density

Powder bed density (PBD) is an important property affecting the process performances and it depends not only on the powder characteristics, but also on the spreading mechanism at play. In this study, PBD was evaluated using cylindrical capsules (Fig. 1a) positioned in different regions of the build plate. Each capsule traps a certain quantity of loose (unfused) powder which is spread during printing, thus allowing post-process measurements of the powder bed density. Once the build is completed, the PBD capsules are detached from the build plate, the support structures removed and the capsules ground to obtain a flat bottom surface. The capsules are then emptied and the masses of the entrapped powder are measured using an analytical balance (Sartorius SECURA324-1S readability 0.1 mg). The empty capsules are then filled with distilled water to measure their volumes and calculate PBDs. The detailed measurement procedure is presented in [26].

2.4.2. Density of printed specimens

The density of printed specimens was measured using Archimedes' technique (ASTM B962–15) with a Sartorius VF4601 density kit and a SECURA324-1S analytical balance with 0.1 mg readability. To this end, cylindrical specimens were weighed in air (m_{air}) and distilled water (m_{water}) mixed with a wetting agent. Their densities were calculated using Eq. (5).

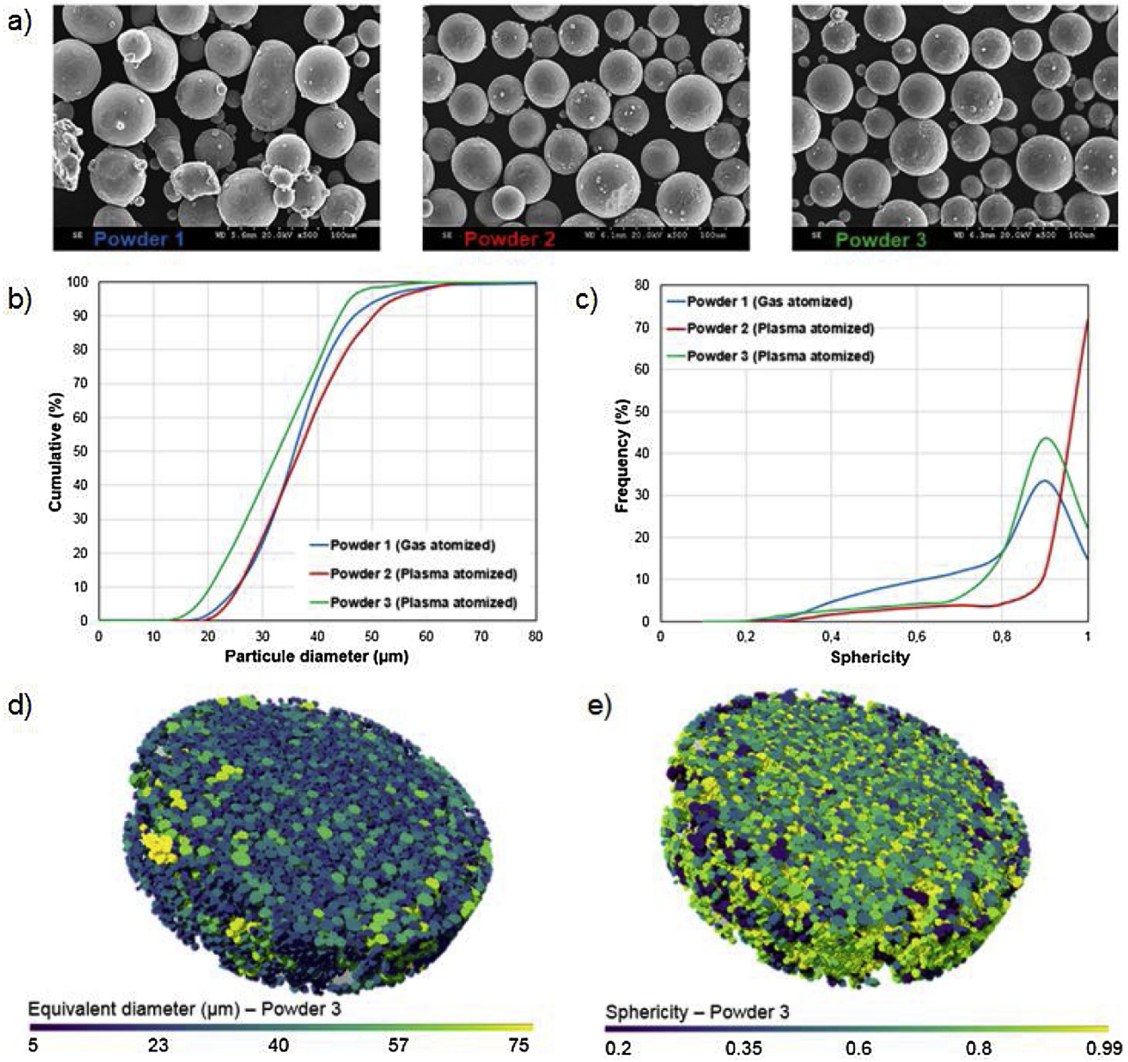

Fig. 3. a) SEM micrographs of Powders 1, 2 and 3); geometric analysis of three powder lots: b) cumulative particle size distributions; c) particle sphericity distributions; d) particle equivalent diameters (Powder 3); e) particle sphericities (Powder 3).

$$\rho = \frac{m_{air}}{m_{air} - m_{water}}\rho_{water} \quad (5)$$

where the water density ρ_{water} was calculated at room temperature (23 °C). Each measurement with a dry/dried specimen was replicated three times.

2.4.3. Surface roughness

A Mitutoyo SJ-402 surface roughness tester equipped with a 12AAB403 standard stylus (tip radius of 5 µm) was used to measure profile roughness arithmetical mean deviations (Ra) on four differently oriented faces of V- shaped specimens (Fig. 1b). Three 4 mm-long linear measurements were performed on each surface of the specimens in the directions parallel to the build direction, according to the ISO 4287:1997 specifications.

2.4.4. Geometric artifacts: minimum printable design features

Geometric artifacts allowing the quantification of minimum printable design features, namely, the minimum achievable walls, sinks and gaps, were printed from each powder lot (Fig. 1c-d-e). A CLEMEX, STC-TC202USB-AH optical microscope (magnification 6.8, accuracy ± 0.03 mm) was used to measure the features of interest.

2.4.5. Tensile properties

Tensile testing was carried out using a Minibionix 858 system (MTS, Eden Prairie, MN, USA) equipped with an MTS 634.12e-25 extensometer and having a crosshead speed of 0.375 mm/min, corresponding to a strain rate of 0.8 s^{-1}. Tensile testing was carried out for each studied configuration in three replicates. Using the generated stress-strain diagrams, the mechanical properties, i.e., the ultimate tensile strength UTS (MPa), the yield strength YS (MPa), the Young's modulus E (GPa), and the elongation at break δ (%) were evaluated.

2.5. Statistical analyses

In order to validate a statistical significance of the results obtained, statistical tests were carried out. The analysis of variance (ANOVA) was used to evaluate whether the differences between three powder lots were significant for a given layer thickness. The student test (*t*-test) was used to compare the results obtained for a given powder lot, but with two different layer thicknesses. The P-values of the F-test (ANOVA) and *t*-test (student) were used as indicators, and where the P-value was smaller than 0.05, the difference between the means of the samples at the 5 % significance level was considered to be statistically significant.

3. Results

3.1. Particle size distribution, morphology, and porosity

In terms of morphology, SEM micrographs (Fig. 3a) show that Powders 2 and 3 are highly spherical, while Powder 1 particles are less regularly shaped. These differences can be explained by the differences in the production routes used, with the plasma atomization (Powders 2 and 3) yielding more spherical particles than the gas atomization (Powder 1), as discussed in [6].

Comparing the PSDs of the selected powder lots (Fig. 3b and Table 4), it can be seen that Powders 1 and 2 have comparable size distributions, while Powder 3 has a wider distribution, which shifts towards fine particles. These observations are further refined by the micro-tomography based analysis (Fig. 3c and Table 4), which points to differences between the two plasma-atomized powders, Powder 3 containing a smaller amount of spherical particles and more irregularly shaped agglomerates of coarse and fine particles than Powder 2.

Fig. 3d,e shows an output example of the Drangonfly software images used to analyze the µCT- generated data where each particle is isolated. Several metrics of interest are calculated and can be visualized in such a 3D representation. (Note the difference in the number of analyzed particles for the SEM and µCT analyses: a few hundred for SEM versus more than ten thousand for µCT, which makes the latter analysis more informative.)

Particle porosities were isolated using the µCT-generated files by detecting the closed pores and reporting the metrics of interest in Table 4. The ratio in percentage between the total number of particles and the particles containing internal pores shows that Powder 2 has the lowest amount of porous particles. Next, the percentage of porosity was calculated by dividing the total volume of pores by the total volume of particles. Powder 3 shows a lower porosity, which correlates with the smaller pore size D_{50} (Table 4). The porosity of Powder 1 was not calculated due to an extremely high amount of open pores.

3.2. Rheological properties

The rheological properties of three powder lots evaluated using Hall and Gustavsson flowmeters and an FT4 powder rheometer are reported in Table 5. The ranking of flow rates obtained using the flowmeters, the calculated Hausner ratio (closer to unity, better flowability), and the Carr index (smaller value, better flowability) correlate with the results of the sphericity evaluation, where more spherical powders (Powders 2 and 3) flow easier through the funnels due to a lower surface friction and mechanical interlocking. Lower flowability of Powder 3 as compared to that of Powder 2 could be explained by a higher amount of fine particles in the former, which increases inter-particles friction and cohesion forces.

The apparent and tapped densities results also correlate with the sphericity of powder particles, where the more spherical Powders 2 and 3 are able to achieve a more efficient packing. The same tendency is observed with a powder rheometer where the differences in particle sphericity can explain the results obtained. The main rheology-generated indices are also reported in Table 5.

The basic flow energy (BFE) represents the energy needed to cut through the powder bed, while the specific energy (SE) provides indications about the mechanical interlocking and the cohesive forces. The lowest BFE and SE values are obtained for Powder 2 and the highest, for Powder 1, pointing to a superior flowability of more spherical powders. The plasma-atomized powders also manifest a higher conditioned bulk density (ρ_c), a lower change in volume (compressibility CI) and a lower permeability (higher pressure drop PD), indicating a more efficient packing state of the particles. The aeration

Table 4
Particle size distribution, sphericity and porosity metrics obtained using µCT analysis.

Powder characteristics		Powder 1	Powder 2	Powder 3
Particle size distribution	D_{10} (µm)	25.3	25.9	20.3
	D_{50} (µm)	35.8	36.7	32.7
	D_{90} (µm)	46.4	50.3	43.9
	Span (6)	0.59	0.66	0.72
Sphericity	D_{10}	0.46	0.64	0.55
	D_{50}	0.79	0.93	0.84
	D_{90}	0.91	0.97	0.93
	Mean	0.73	0.88	0.79
	Std deviation	0.18	0.15	0.16
	Span (6)	0.57	0.35	0.45
Particles porosity	Ratio (%) (7)	3.50	1.07	3.15
	Porosity (%) (8)	–	1.88	0.12
	Pores mean sphericity	–	0.50	0.50
	Pores D_{50} (µm)	–	4.50	2.97

Span = $D_{90} - D_{10}/D_{50}$ (6).
Ratio (%) = *Number of porous particles/Total number of particles* (7).
Porosity (%) = *Total volume of pores/Total volume of particles* (8).

Table 5
Summary of the rheological properties of three powder lots.

Measurement technique	Powder characteristics	Powder 1	Powder 2	Powder 3
Hall flowmeter	Flow rate (s/50 g)	35 ± 0.416	25 ± 0.07	26 ± 0.05
Gustavson flowmeter	Flow rate (s/50 g)	58.1 ± 2.42	31.8 ± 0.36	52.8 ± 0.63
Bulk measurement	Apparent density (g/cm^3)	2.39 ± 0.012	2.61 ± 0.015	2.58 ± 0.016
	Tapped density (g/cm^3)	2.55 ± 0.022	2.72 ± 0.017	2.70 ± 0.00
	Hausner ratio [9]	1.07	1.04	1.05
	Carr index (%) [10]	6.27	4.21	4.44
FT4 powder rheometer	Basic flow energy (mJ)	293.5 ± 13.8	265.4 ± 3.8	280.4 ± 14.3
	Specific energy (mJ/g)	2.85 ± 0.03	1.61 ± 0.01	1.73 ± 0.06
	Bulk density (g/cm^3)	2.49 ± 0.02	2.71 ± 0.01	2.68 ± 0.01
	Compressibility index (%)	2.42 ± 0.05	1.69 ± 0.01	1.88 ± 0.05
	Pressure drop (mBar)	5.41 ± 0.32	6.54 ± 0.21	6.33 ± 0.32
	Aeration energy (mJ)	23.79 ± 6.15	6.86 ± 0.4	8.48 ± 2.04
	Cohesion coeff. (kPa)	0.39 ± 0.082	0.25 ± 0.007	0.28 ± 0.01

Hausner ratio = *Tapped density*/*Apparent density* (9).
Carr index = 100 *(*Tapped density* − *Apparent density*)/*Tapped density* (10).

energy (AE) indicates the energy needed to overcome the mechanical interlocking and cohesive forces, the highest value being obtained for the less spherical gas-atomized Powder 1. The cohesion coefficient (*c*) obtained during shear testing is the lowest for Powders 2 and 3, thus indicating that more spherical powders are more ready to transition from a static consolidated state to a dynamic state of flow. It can finally be seen that the more spherical plasma-atomized Powders 2 and 3 manifest a globally superior flowability as compared to the less spherical gas-atomized Powder 1.

To sum up the results obtained, Fig. 4 shows a radar diagram of the normalized FT4-generated indices for three powder lots studied. In accordance with the criteria defined in Table 2, the smaller the area covered by the diagram, the higher the powder suitability for the LPBF process. According to this diagram (Fig. 4), the powder LPBF suitability ranges from higher to lower as Powder 2, Powder 3 and Powder 1; the difference between the first two being much less significant than between them and Powder 1.

In order to express the overall suitability of three powder lots for LPBF using the FT4-generated indices, it is proposed to calculate a figure of merit called "AMS" (referring to AM suitability). To this end, each FT4-generated index is normalized according to the maximum value obtained among all the powder lots studied, and the normalized indexes are then combined to build an objective function (11), which needs to be minimized. As a first approximation, all the importance weights of Eq. (11) are taken equal, and their sum corresponds to unity.

$$AMS = \left(\frac{1}{\rho_c} + CI + PD + SE + AE + BFE + c\right)/7 \quad (11)$$

where ρ_c is the conditioned bulk density; CI, the compressibility index; PD, the pressure drop; SE, the specific energy; AE, the aeration energy; BFE, the basic flow energy, and c, the cohesion coefficient. Table 6 shows the calculated AM suitability factors (AMS) of each powder lot and the corresponding normalized cumulative errors. The smaller the AMS, the more suitable the powder is for the LPBF process, according to the criteria previously defined. Based on these assumptions, Powder 2 appears to be 5.5 % more suitable for the LPBF process than Powder 3, and 26.5 % more suitable for this process than Powder 1.

3.3. Powder bed density

Using capsule specimens (Fig. 1a), which entrap powder during the build, the powder bed density obtained with three powder lots using two layer thicknesses (30 and 60 μm), is evaluated. Since, in each job, six capsules were placed on the build plate in different regions as shown in Fig. 2, the average powder bed densities and the corresponding standard deviations were calculated, normalized according to the alloy theoretical density (4.41 g/cm^3), and are reported in Fig. 5 and Table A1 (Appendix A).

It must be noted that for a given layer thickness, the differences in powder bed densities between three powder lots are statistically significant. For each powder lot however, the difference in powder bed densities obtained with two different layer thicknesses is statistically insignificant.

The powder bed densities of different lots are close to 60 % of the theoretical density of Ti-6Al-4V alloy. For a layer thickness of 60 μm, the highest density is obtained with Powder 2, which is 5.1 % and 4.7 % higher than those with Powder 1 and Powder 3, respectively. For a 30 μm layer thickness, the highest density is also obtained with Powder 2, but the gain becomes less significant: the density of Powder 2 is 2.1 % and 0.5 % higher than those with Powder 1 and Powder 3, respectively. The results obtained follow the same trend as that observed with the rheological properties, but the differences become much less pronounced: ~26 % difference between Powders 1 and 2 in terms of powder flowability transforms to only ~5 % difference, in terms of powder bed density.

The apparent and tapped densities, firstly reported in Table 5, are normalized according to the theoretical density of the alloy and included in Table A1 (Appendix A). It can be seen that a value of apparent density cannot be used to approximate the powder bed density with sufficient fidelity. Closer values are obtained with the tapped density, but the impact of a layer thickness cannot be estimated using this metric.

The fact that the thinner the layer, the greater the powder bed density can be explained by the size of particles in the powder bed formed by layers of different thicknesses, as discussed in [12,26,31].

For thinner layers, during spreading, a greater amount of larger particles are dragged by the doctor blade to the receiving container,

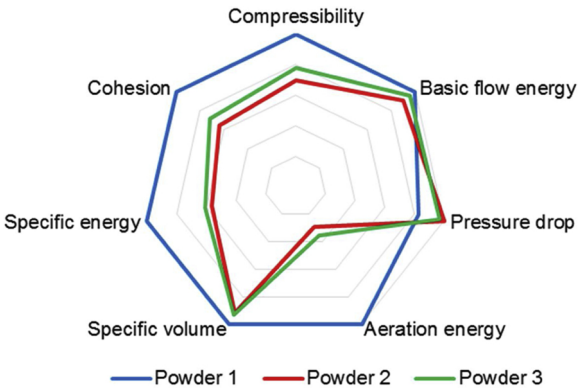

Fig. 4. Radar diagram comparing the rheological properties of three studied powder lots.

Table 6
AM suitability factors (AMS) of three powder lots of this study.

	Powder 1	Powder 2	Powder 3
AMS	0.975 ± 0.09	0.717 ± 0.01	0.759 ± 0.04

thus in turn leaving a greater amount of finer particles in the powder bed, which leads to a tighter packing and, hence, to a higher powder bed density. A further analysis of the particle size distribution in powder samples from the collector duct of the LPBF machine could confirm or infirm the previously presented explanation.

In terms of sensitivity to the layer thickness variation, Powder 2 shows the most stable behavior with a variation of 1.4 %, while the highest sensitivity is obtained with Powder 3 with a variation of 2.9 %, which could be due to the presence of a higher amount of fine particles that tend to agglomerate in a less predictable way, thus leading to less regular results. This can also be seen from a larger scatter of Powder 3 results.

3.4. Densities of printed specimens

The averages and the standard deviations of densities of printed cylindrical specimens obtained for different testing configurations are normalized according to the theoretical density of the alloy (4.41 g/cm^3) and reported in Fig. 6 and in Table A2 (Appendix A). LPBF printing with three powder lots and two layer thicknesses led to the production of highly dense specimens (> 99 %). The highest printed densities were obtained with the plasma-atomized Powders 2 and 3, thus correlating with the powder bed densities (Fig. 5).

In order to validate the statistical significance of the results obtained, statistical tests were carried out. The P-values are reported in Table A2 (Appendix A), and the results smaller than 0.05 are highlighted. It must be noted that for a layer thickness of 30 µm, the differences in printed densities obtained with three powder lots are significant, but for a layer thickness of 60 µm, it is not the case, given a larger scatter in density values observed with a thicker layer. Next, for all the powders, the thicker the layer, the lower the part density. Note, however, that for Powders 2 and 3, the differences in printed densities corresponding to different layer thicknesses are statistically significant, while for Powder 1, this difference is not statistically significant.

3.5. Surface roughness

Using V-shaped specimens (Fig. 1-b) containing four planar faces oriented with respect to the build plate under angles of 0, 45, 90 and 135°, the average surface roughness R_a (µm) and the corresponding standard deviations are calculated and reported in Fig. 7 and in Table B1 (Appendix B). For each configuration (build orientation and layer thickness), the surface roughness values are normalized according to their respective maxima, and the normalized average surface roughnesses are calculated. The sensitivity of the surface roughness to the layer thickness variations is also estimated for each powder lot.

The observed surface roughness variations between the differently oriented surfaces can be explained by several phenomena discussed in (Strano, Hao et al. 2013). The horizontal surfaces (0°) manifest the smoothest finish, since the measurements are made on a single layer of fused powder. Higher roughnesses of the up-face inclined surfaces (45 and 90°) are due to a so-called staircase effect. The down-faced inclined surfaces (135°) are not supported during printing, thus leading to poor heat dissipation and sintering of adjacent particles, which result in the lowest surface quality.

Statistical tests have been carried out to compare the results of these different testing configurations. The highlighted cells in the tables below the graphs in Fig. 7 indicate a significant difference at the 5 % significance level. Highlighted cells in the first row mean that the results are significantly different between the three powders for the considered configuration. Highlighted cells in the second row mean that the results are significantly different between the two layer thicknesses for the considered configuration (powder/surface orientation). The corresponding P-values are reported in Table B1 (Appendix B). When considering each configuration separately, it can be seen that the differences are significant for most of the cases of the inclined surfaces (45 and 135°) but are less pronounced for the other building orientations. The layer thickness variation does not seem to significantly affect the R_a results.

The differences in the surface roughness values obtained with different powder lots can be explained by the differences in their powder bed densities where the presence of voids between the particles negatively affect the surface finish. LPBF with Powder 2 results in a surface finish 17 % smoother than with Powder 1 and 10.8 %, with Powder 3. Powder 2 also shows the smallest sensitivity to the layer thickness variation.

In order to facilitate the comparison, box plots combining the surface roughness results of the differently-oriented surfaces for each configuration studied (powder/layer thickness) are presented in Fig. 8. It can be seen that the use of Powder 2 resulted in the lowest surface roughness followed by Powder 3 and, finally, Powder 1. By comparing the values of the first and third quantiles (Q1 and Q3 in Fig. 8), it can be seen that the surface finish obtained with the plasma-atomized powders (Powders 2 and 3) with a layer thickness of 60 µm is better than the one obtained with the less-spherical Powder 1 with a layer thickness of 30 µm.

3.6. Geometric attributes: minimum printable design features

Using the artifacts presented in Fig. 1c-d-e, geometric attributes of interest, i.e., the minimum achievable sink, gap and wall thicknesses, were evaluated. The design features have thicknesses ranging from 0.1 to 2 mm. More details are included in Tables B2–B4 (Appendix B).

As far as the minimum printable gaps are concerned, their values

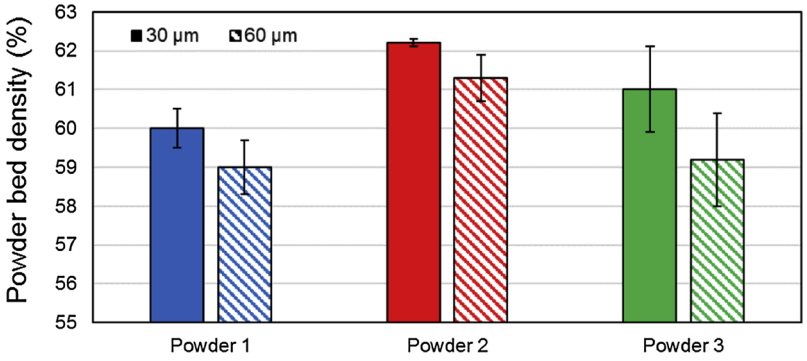

Fig. 5. Powder bed densities of three powder lots for two layer thicknesses.

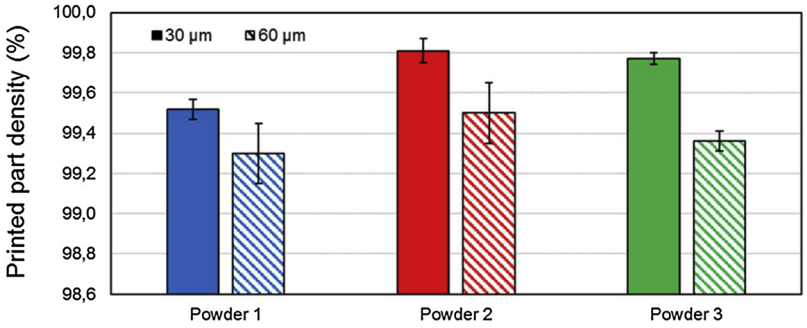

Fig. 6. Densities of specimens printed from three powder lots with two layer thicknesses.

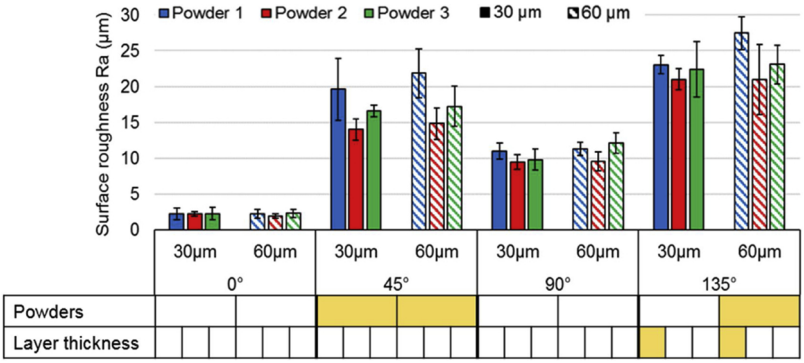

Fig. 7. Average surface roughness R_a (µm) measured on V-shaped specimens with differently-oriented surfaces printed from three powder lots; highlighted cells indicates values which differ significantly in terms of their statistical analysis.

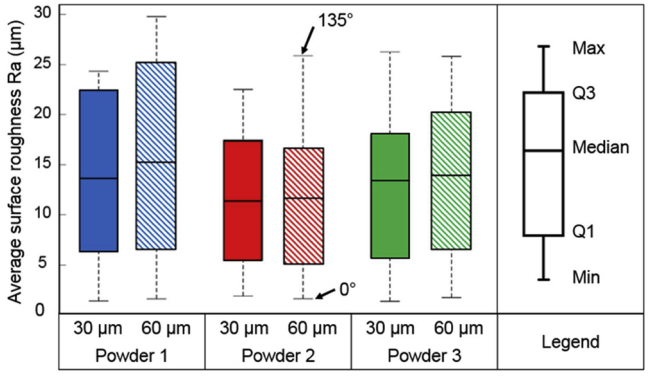

Fig. 8. Box plots of average surface roughness Ra (µm) measured on V-shaped specimens with differently-oriented surfaces printed from three powder lots; arrows point to extreme surface roughness values corresponding to 0° and 135° build orientation angles.

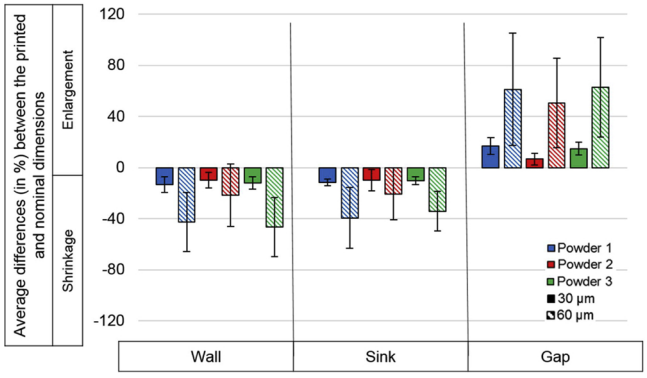

Fig. 9. Average differences (in %) between the printed and nominal dimensions.

correspond to 0.1 mm, irrespective of the powder lot and the layer thickness. The minimum printable values of sinks and walls are identical for three powder lots, but the thicker the layer, the larger these values: for a layer thickness of 30 µm, the minimum printable sink (wall) is 0.3 mm, whereas for a layer thickness of 60 µm, it is 0.5 mm. Fig. 9 shows the average differences in percentage between the nominal dimensions (CAD) and the measured dimensions of the artifacts printed, -per layer thickness and per powder lot.

The difference in percentage per layer thickness shows that the thicker the layer, the less accurate the printing. The differences in percentage per powder lot show that Powder 2 manifests the smallest variance in respect to the nominal dimensions. Powder 2 allows printing 43 % more accurate walls, 40 % more precise sinks and 29 % more accurate gaps than Powder 1, and 46 % more accurate walls, 31 % more precise sinks and 38 % more accurate gaps than Powder 3. The differences between Powders 1 and 3 are below 5 % for the walls and the gaps and around 13 % for the sinks.

3.7. Tensile properties

The ultimate tensile strength UTS (MPa), the yield strength YS (MPa), the elongation at break δ (%), and the Young's modulus E (GPa) were evaluated for different configurations studied (3 powder lots, 2 layer thicknesses, 2 build orientations). For each property, the average and the corresponding standard deviation values are shown in Fig. 10 for the as-built specimens (Fig. 10a-c-e) and the heat-treated specimens (Fig. 10b-d-f). The numerical values can be found in Tables C1–C4 (Appendix C). It should be noted that the results for Powder 2 with a layer thickness of 60 µm in the as-built conditions for the horizontal build orientation are not reported since these specimens were highly

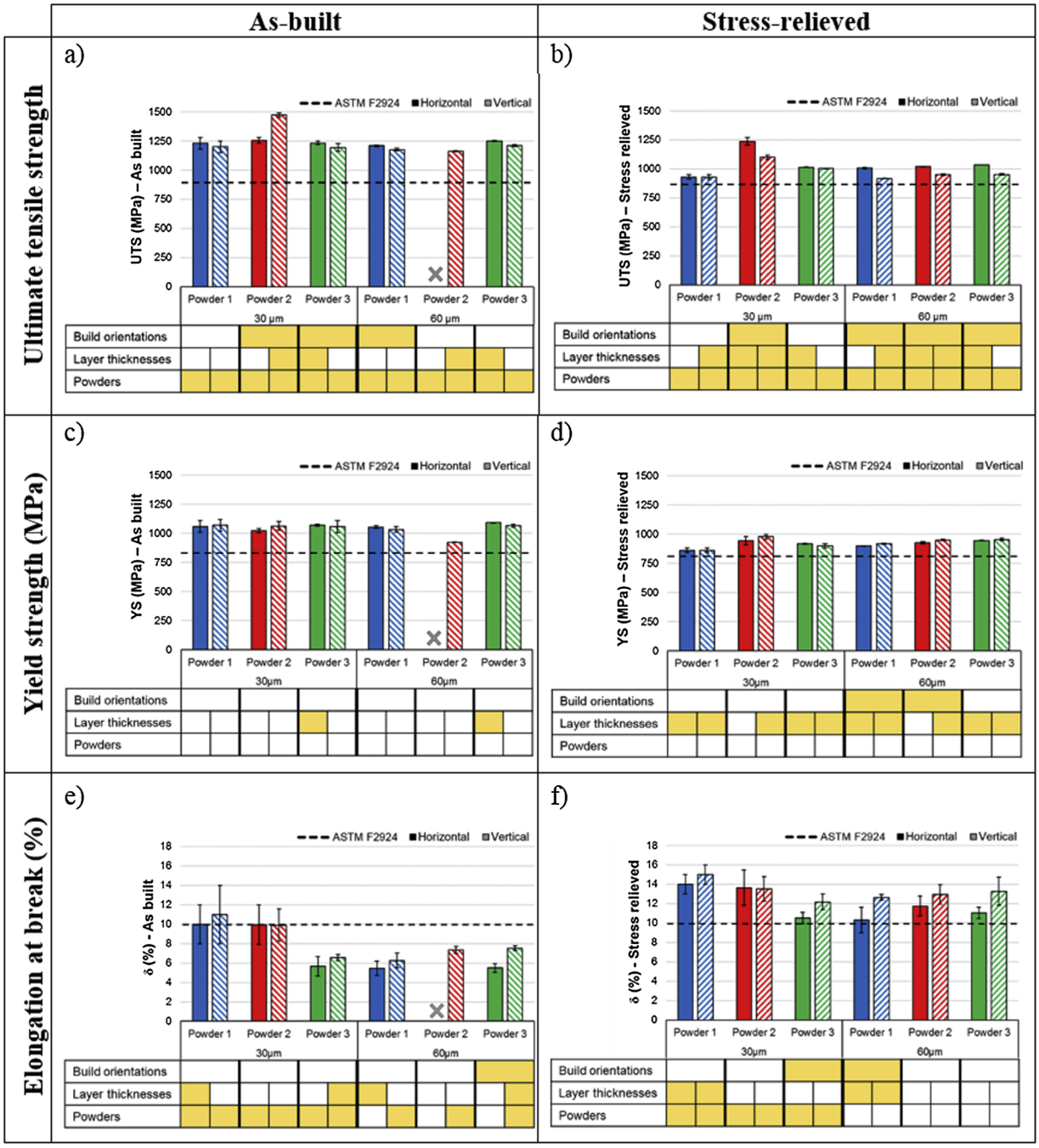

Fig. 10. Mechanical properties of three powder lots for the as-built and stress-relieved states: a) UTS (as-built), b) UTS (stress-relieved), c) YS (as-built), d) YS (stress-relieved), e) δ (as-built), f) δ (stress-relieved).

bent due to residual stresses, and because their machining resulted in an uneven thickness along their longitudinal axis.

Note that for all the studied configurations, the ultimate tensile and yield strength values are higher than the requirements presented in ASTM F2924-14 (UTS > 895 MPa and YS > 825 MPa). Note also that in the as-built state, most of the specimens fail to reach the elongation at break requirement of δ > 10 % (ASTM F2924-14), but after stress relief heat treatment, they meet this minimum condition (see dotted lines on graphs in Fig. 10).

In order to compare the results for the different configurations studied, the analysis of variance and the student test were carried out. Highlighted cells in the tables below the graphs in Fig. 10 indicate a significant difference at the 5 % significance level. The P-values are reported in Tables C1–C4 (Appendix C).

Highlighted cells in the first row of the tables under the graphs mean that the results are significantly different between the horizontal and vertical build orientations. Highlighted cells in the second row of the table indicate a significant difference between the two layer thicknesses for each configuration (powder/build orientation). Highlighted cells in the third row indicate a significant difference between the three powders for each build orientation and each layer thickness. It can be seen that for most of the cases with a layer thickness of 30 µm, the differences between the three powder lots are significant in terms of the mechanical properties studied. For a layer thickness of 60 µm, for the Young's modulus, and the elongation at break, these differences are not statistically significant.

The variation in the layer thickness does not affect the Young's modulus. For the yield strength, the differences are significant for the

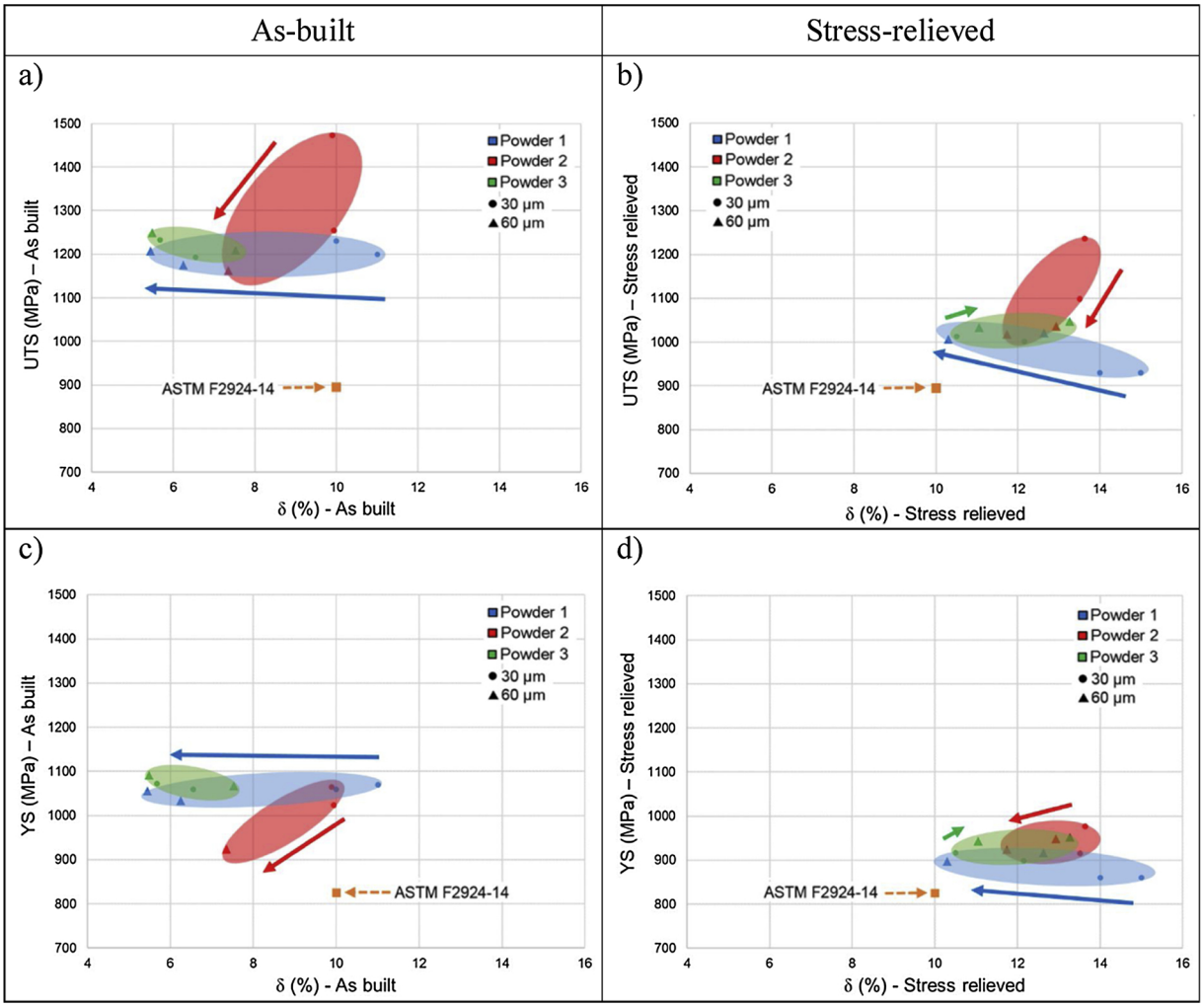

Fig. 11. Ultimate tensile strength and yield strength in respect to the elongation at break for three powder lots in the as-built and stress-relieved states: a) UTS (δ), as-built, b) UTS (δ), stress-relieved, c) YS (δ), as-built, d) YS (δ), stress-relieved; arrows indicate towards an increase in layer thickness.

stress-relieved samples, but less pronounced for the as-built samples. No clear trend can be identified for the ultimate tensile strength and the elongation at break. Regarding the impact of build orientations (horizontal "XY" and vertical "Z"), it can be seen that the ultimate tensile strength is the property most sensitive to the build orientation variation. In some cases, the anisotropy is less pronounced when using a thinner layer thickness.

To sum up the most relevant results, the ultimate tensile strength (UTS) and the yield strength (YS) are plotted as functions of the elongation at break (δ) for the as-built and stress-relieved specimens in Fig. 11. The ASTM F2924-14 requirements are represented by the orange square marks. The triangles and the circles represent the results obtained respectively with layer thicknesses of 60 µm and 30 µm. The shaded colored areas encompassing the results of each powder lot were added to facilitate the reading of the graphs. The arrows point toward the results obtained with a thicker layer; the absence of an arrow indicates that no clear trend could be observed when increasing the layer thickness.

In the UTS (δ) graph for the as-built specimens (Fig. 11a), it can be seen that Powder 2 manifests superior mechanical properties, where an increase in the layer thickness causes a ~20 % decrease in resistance and a 25 %, in ductility. An increase in the layer thickness with Powder 1 does not drastically affect the resistance, but greatly influences the ductility, with a decline of 43 %. Powder 3 shows good resistance, reduced ductility and low sensitivity to the layer thickness variation. In the YS (δ) graph for the as-built specimens (Fig. 11c), Powders 1 and 3 show the same trends as in the UTS (δ) graph (Fig. 11a), but Powder 2 manifests a certain decrease in the material resistance, especially for the 60 µm layer thickness.

In the UTS (δ) graph for the stress-relieved specimens (Fig. 11b), Powder 2 manifests superior mechanical properties, where an increase in the layer thickness results in a ~10 % decrease in resistance and an 8.5 % decrease in ductility. Powder 1 shows the lowest resistance and the highest sensitivity to the layer thickness variation (20 % in ductility). Powder 3 shows middle-range results, with a relatively low sensitivity to the layer thickness variation. In the YS (δ) graph (Fig. 11d), the same trends are observed, but with a less pronounced difference between the three powders studied.

4. General discussion

This study demonstrated that more spherical powders manifest better flowability, while the presence of a higher amount of fine particles negatively affects this behavior, both observations being in accordance with the literature data [5,6]. In order to express the overall suitability of three powder lots for LPBF from a rheological point of view, a figure of merit "AMS" was established based on the FT4-generated indices. The current "AMS" formulation uses equal importance weight for the different indices. Additional studies with other powder lots are required in order to identify the most relevant FT4-generated

indices and set the importance weight accordingly, and prove the effectiveness of this newly established index as an indicator of the powders' LPBF suitability. Next, the powder bed density measured using capsules entrapping the powder during the build demonstrated that for all three powder lots, the obtained values varied about 60 % of the alloy theoretical density. Here too, the use of more spherical powders resulted in more dense powder beds, showing the same trend observed with the rheological tests, but this time with less significant differences.

Next, all the specimens printed from three powder lots showed densities exceeding 99 % and once again, the same trend was observed where more spherical powders resulted in more dense specimens. In terms of the surface finish, a clear correlation between the surface roughness and the powder bed density was observed for different surface orientations, favoring more spherical Powder 2 with a smaller amount of fine particles. It should be noted that the surface finish obtained with Powder 2 (layer thickness of 60 µm) is better than that with Powder 1 (layer thickness of 30 µm), thus indicating that using powders with more spherical particles allows increasing the build rate, while obtaining equivalent or superior results. Next, artifacts allowing measuring geometric properties of interest (minimum printable design features) were printed, and again, more spherical powder showed better results.

Finally, the mechanical properties of specimens printed from three powder lots were compared for different build orientations, layer thicknesses and post-treatments. The more spherical plasma-atomized powder (Powder 2) showed superior mechanical properties overall. It should be noted that the plasma-atomized powders (Powders 2 and 3) with a layer thickness of 60 µm outperformed the parts printed with the gas-atomized powder (Powder 1) with a layer thickness of 30 µm in terms of their mechanical resistance. This provides again an option to increase the process productivity, while yielding components with similar or better properties. Next, significant differences observed between Powders 1 and 3 in terms of their morphology (Table 4) and rheological properties (Table 5) resulted in much less pronounced differences in terms of the mechanical properties of parts printed with these powders.

Several hypotheses could explain these observations, the first being the robustness of the process and its low sensitivity to slight variations in powder characteristics, as discussed in [5], where Ti-6Al-4 V powders with slightly different particle morphologies yielded comparable mechanical properties [32] and who compared Ti-6Al-4 V powders with different particle size distributions and also recorded equivalent mechanical performances.

The second explanation is based on the known fact that thermal conductivity of the powder bed depends on the powder characteristics (size distribution, morphology, surface area), thus affecting the laser-matter interaction [32]. That means that the use of identical printing parameters for the three powder lots of this study could result in sub-optimal results for some of them. It is reasonable to suppose that if processing parameters were optimized for each powder, that would have maximized the mechanical properties and, therefore, enhanced the differences between the powders, as discussed in [33].

Before definite conclusion is reached, further studies needs to be carried out. An interesting aspect would be to study the fatigue resistance of parts manufactured with the three powder lots of this study in order to assess whether the detected variations in powder characteristics affect the fatigue properties more than they affect their static equivalents [34]. Another area of interest could be the investigation of shear forces applied on parts during the recoating operation, which is especially important for delicate and small-featured components, such as lattice structures, and where the powder flowability can affect the stability of these builds.

Moreover, it is important to study whether a superior flowability of spherical powders will allow increasing the speed of powder recoating, without significantly affecting the density and the uniformity of the powder bed. If we consider that recoating time represents of up to 50 % of the total build time, depending on the number, geometrical complexity and build orientations of printed parts [35], reducing this time could result in significant gains in process productivity.

Finally, despite the differences in the obtained properties, the powder selection process is highly driven by the purchase costs of the powder lots. The decision is up to the clients depending on their needs and their budgets to decide whether the difference in parts properties is worth the difference in powder prices.

5. Conclusions

Three Ti-6Al-4 V powder lots where selected to investigate the impact of particle morphology and size distribution on the powder flowability and the LPBF process performances in terms of powder bed density, as well as density, surface roughness, accuracy, printability limits and mechanical properties of the printed parts. It was shown that a more spherical powder (Powder 2) exhibits a better rheological behavior and a more efficient particle packing, favoring the formation of a highly dense powder bed and yielding printed parts with superiors densities, surface finish and dimensional accuracy. The presence of a greater amount of fine particles (Powder 3) negatively affects the previously mentioned properties due to higher inter-particle friction.

The highly spherical plasma-atomized Powder 2 showed superior mechanical properties, whereas the less spherical gas-atomized Powder 1 showed the highest sensitivity to layer thickness variations overall. Differences in the mechanical properties observed in this study were much less significant than those in the powder flowability, surface finish and accuracy of printed parts. The significance of the differences observed was supported by statistical analyses.

Funding

The financial support of Natural Sciences and Engineering Research Council of Canada (NSERC) and PyroGenesis Additive Canada is gratefully acknowledged.

Authors' contributions

The work plan was established by SE. Brika and M. Letenneur to meet the study objectives defined by V. Brailovski and C. Dion. Powders selection was carried out by all the coauthors based on the state of the art and industrial partners' needs. Micro-tomography scans were carried by M. Letenneur and analyzed by SE. Brika. Rheological testing of the selected powders was done by SE. Brika. The design, fabrication and testing were performed by SE. Brika with the aid of M. Letenneur. V. Brailovski contributed to the results interpretation and manuscript drafting.

Declaration of Competing Interest

The authors declare no conflicts of interest.

Acknowledgments

The authors would like to express their appreciation for the support provided by Freeman technology and Object Research Systems (ORS) Inc. and to thank M. Samoilenko, A. Timercan, N. Mohhamadian and O. Bourdeau-Rousseau for their assistance during this project.

Appendix A. Powder bed and part densities

Table A1
Powder bed density (%) of three powder lots with two layer thicknesses.

Powder characteristics	Powder 1	Powder 2	Powder 3
Powder bed density (%) for a layer thickness of:			
30 μm	60.0 ± 0.5	62.2 ± 0.1	61.0 ± 1.1
60 μm	59.0 ± 0.7	61.3 ± 0.6	59.2 ± 1.2
Variation 30–60 μm (%)	1.7	1.4	2.9
Apparent density (%)	54.2 ± 0.003	59.2 ± 0.003	58.5 ± 0.004
Tapped density (%)	57.8 ± 0.005	61.7 ± 0.004	61.2 ± 0.0

Table A2
The densities of printed specimens obtained for the different configurations tested.

	Printed specimen densities, %			
	Powder 1	Powder 2	Powder 3	
30	99.52 ± 0.05	99.81 ± 0.06	99.77 ± 0.03	***0.0006***
60	99.30 ± 0.15	99.50 ± 0.15	99.36 ± 0.05	0.2165
t-test (p-value)	0.0735	***0.0293***	***0.0002***	

Appendix B. Geometric properties

Table B1
Average surface roughness Ra (μm) of the studied powder lots.

		Surface roughness R_a (μm)			*F-test*
Surface angle (°)	Layer thickness (μm)	Powder 1	Powder 2	Powder 3	*(p-value)*
0	30	2.22 ± 0.8	2.21 ± 0.3	2.26 ± 0.9	0.9963
	60	2.23 ± 0.6	1.93 ± 0.3	2.29 ± 0.5	0.6539
	t-test (p-value)	0.9935	0.3055	0.9549	
45	30	19.61 ± 1.9	14.00 ± 1.5	16.59 ± 0.9	***0.0103***
	60	21.84 ± 2.2	14.83 ± 2.2	17.25 ± 2.4	***0.0229***
	t-test (p-value)	0.2544	0.6157	0.6702	
90	30	10.97 ± 1.1	9.45 ± 1.0	9.79 ± 1.5	0.3365
	60	11.32 ± 0.9	9.56 ± 1.3	12.10 ± 1.5	0.1097
	t-test (p-value)	0.6923	0.9135	0.1260	
135	30	23.05 ± 1.3	21.00 ± 1.5	22.41 ± 2.1	0.3666
	60	27.45 ± 2.3	20.96 ± 2.1	23.08 ± 1.9	***0.0245***
	t-test (p-value)	***0.0455***	0.9798	0.6992	
Normalized average, Ra		0.99 ± 0.01	0.82 ± 0.02	0.92 ± 0.01	
Average variation 30-60 μm (%)		7.39	4.92	6.86	

Table B2
Difference in percentage between the printed walls and their nominal dimensions.

	Difference in % for walls thicknesses					
	Powder 1		Powder 2		Powder 3	
Nominal dimensions (mm)	30 μm	60 μm	30 μm	60 μm	30 μm	60 μm
0.1	X	X	X	X	X	X
0.2	X	X	X	X	X	X
0.3	–21.3	X	–15.7	X	–18.1	X
0.4	–20.5	X	–12.5	X	–16.2	X
0.5	–18.5	–58.9	–10.6	–54.8	–10.5	–65.2
0.6	–14.7	–66.2	–19.9	–43.4	–12.0	–68.6
0.8	–10.0	–61.0	–7.1	–28.9	–9.6	–58.8
1	–8.7	–37.6	–5.5	–9.9	–17.7	–49.3
1.5	–7.3	–22.8	–4.0	+0.5	–9.4	–25.5
2	–6.3	–9.7	–3.5	+6.1	–4.2	–11.2
Difference per layer thickness (%)	–13.4	–42.7	–9.8	–21.7	–12.2	–46.4
Difference per powder lot (%)	–28.0		–15.8		–29.3	

Table B3
Difference in percentage between the printed sinks and their nominal dimensions.

	Difference in % for sinks					
	Powder 1		Powder 2		Powder 3	
Nominal dimensions (mm)	30 μm	60 μm	30 μm	60 μm	30 μm	60 μm
0.1	X	X	X	X	X	X
0.2	X	X	X	X	X	X
0.3	–15.0	X	–22.1	X	–6.9	X
0.4	–10.0	X	–18.9	X	–15.8	X
0.5	–15.0	–45.6	–16.4	–43.5	–10.8	–53.4
0.6	–11.7	–66.5	–9.6	–41.3	–10.7	–31.6
0.8	–11.3	–58.4	–6.5	–26.7	–11.8	–45.3
1	–13.0	–45.3	–5.1	–15.7	–5.5	–40.6
1.5	–8.3	–15.0	–0.5	–2.2	–9.7	–23.8
2	–8.0	–6.5	–0.4	+5.9	–9.5	–10.3
Difference per layer thickness (%)	–11.5	–39.6	–9.9	–20.6	–10.1	–34.2
Difference per powder (%)	–25.5		–15.2		–22.1	

Table B4
Difference in percentage between the printed gaps and their nominal dimensions.

	Difference in % for gaps					
	Powder 1		Powder 2		Powder 3	
Nominal dimensions (mm)	*30 μm*	*60 μm*	*30 μm*	*60 μm*	*30 μm*	*60 μm*
0.1	+29.0	+159.0	+9.0	+135.0	+23.0	+147.5
0.2	+23.5	+113.7	+6.0	+76.5	+19.0	+116.2
0.3	+19.3	+70.3	+0.7	+69.0	+20.0	+61.7
0.4	+17.0	+67.5	+1.3	+42.0	+14.0	+52.2
0.5	+19.6	+45.4	+1.4	+40.3	+18.2	+51.8
0.6	+12.8	+38.0	+4.8	+38.2	+11.3	+55.2
0.8	+10.6	+33.8	+10.0	+36.5	+10.8	+47.8
1	+16.9	+32.3	+12.4	+26.5	+15.6	+36.8
1.5	+8.0	+27.2	+8.3	+22.9	+6.6	+30.6
2	+11.3	+23.3	+12.1	+18.8	+10.2	+26.6
Difference per layer thickness (%)	+16.8	+61.0	+6.6	+50.6	+14.9	+62.6
Difference per powder (%)	+38.9		+28.5		+38.7	

Appendix C. Mechanical properties

Table C1
Ultimate tensile strength UTS (MPa).

Layer thickness (μm)	Build orientation	Post treatment	Powder 1	Powder 2	Powder 3
30	Z	SR	930 ± 20	1099 ± 16	1001 ± 4
		AB	1200 ± 50	1473 ± 19	1193 ± 32
	XY	SR	930 ± 20	1236 ± 33	1013 ± 3
		AB	1230 ± 50	1255 ± 25	1233 ± 14
60	Z	SR	916 ± 2	1036 ± 6	1048 ± 5
		AB	1176 ± 11	1162 ± 3	1208 ± 9
	XY	SR	1006 ± 7	1019 ± 4	1034 ± 0
		AB	1208 ± 5	–	1249 ± 5

Table C2
Yield strength YS (MPa).

Layer thickness (μm)	Build orientation	Post treatment	Powder 1	Powder 2	Powder 3
30	Z	SR	860 ± 20	976 ± 19	898 ± 18
		AB	1070 ± 50	1064 ± 37	1059 ± 54
	XY	SR	860 ± 20	943 ± 34	916 ± 6
		AB	1060 ± 50	1024 ± 18	1073 ± 8
60	Z	SR	916 ± 6	949 ± 6	952 ± 10
		AB	1034 ± 24	925 ± 3	1067 ± 15
	XY	SR	897 ± 3	925 ± 8	944 ± 3
		AB	1056 ± 11	–	1092 ± 4

Table C3
Elongation at break δ (%).

Layer thickness (μm)	Build orientation	Post treatment	Powder 1	Powder 2	Powder 3
30	Z	SR	15 ± 1	14 ± 1.3	12 ± 0.8
		AB	11 ± 3	10 ± 1.7	7 ± 0.3
	XY	SR	14 ± 1	14 ± 1.8	11 ± 0.6
		AB	10 ± 2	10 ± 2	6 ± 1
60	Z	SR	13 ± 0.3	13 ± 1.0	13 ± 1.4
		AB	6 ± 0.8	7 ± 0.4	8 ± 0.2
	XY	SR	10 ± 1.3	12 ± 1.0	11 ± 0.6
		AB	5 ± 0.7	–	5 ± 0.5

Table C4
Young modulus E (GPa).

Layer thickness (μm)	Build orientation	Post treatment	Powder 1	Powder 2	Powder 3
30	Z	SR	114 ± 9	118 ± 2	113 ± 1
		AB	110 ± 10	131 ± 5	107 ± 7
	XY	SR	116 ± 9	124 ± 6	118 ± 5
		AB	110 ± 10	109 ± 2	112 ± 2
60	Z	SR	116 ± 5	119 ± 4	114 ± 4
		AB	110 ± 7	114 ± 1	115 ± 8
	XY	SR	112 ± 4	114 ± 4	114 ± 3
		AB	108 ± 6	–	110 ± 3

References

[1] T. Wohlers, R.I. Campbell, Wohlers Report 2017: 3D Printing and Additive Manufacturing State of the Industry: Annual Worldwide Progress Report, Wohlers Associates, Incorporated, 2017.

[2] S. Sun, M. Brandt, M. Easton, Powder bed fusion processes: an overview, Laser Addit. Manuf. Elsevier, 2017, pp. 55–77.

[3] M. Letenneur, V. Brailovski, A. Kreitcberg, V. Paserin, I. Bailon-Poujol, Laser powder bed fusion of water-atomized iron-based powders: process optimization, J. Manuf. Mater. Process. 1 (2017) 23.

[4] A. Rogalsky, I. Rishmawi, L. Brock, M. Vlasea, Low cost irregular feed stock for laser powder bed fusion, J. Manuf. Processes 35 (2018) 446–456.

[5] V. Seyda, D. Herzog, C. Emmelmann, Relationship between powder characteristics and part properties in laser beam melting of Ti–6Al–4V, and implications on quality, J. Laser Appl. 29 (2017) 22311.

[6] G. Chen, S.Y. Zhao, P. Tan, J. Wang, C.S. Xiang, H.P. Tang, A comparative study of Ti-6Al-4V powders for additive manufacturing by gas atomization, plasma rotating electrode process and plasma atomization, Powder Technol. 333 (2018) 38–46.

[7] N.P. Karapatis, G. Egger, P.E. Gygax, R. Glardon, Optimization of powder layer density in selective laser sintering, Proc. Solid Free. Fabr. Symp. 1999 (1999) 255–263.

[8] A.B. Spierings, G. Levy, Comparison of density of stainless steel 316L parts produced with selective laser melting using different powder grades, Proc. Annu. Int. Solid Free. Fabr. Symp. Austin, TX, 2009, pp. 342–353.

[9] A. Strondl, O. Lyckfeldt, H. Brodin, U. Ackelid, Characterization and control of powder properties for additive manufacturing, JOM 67 (2015) 549–554.

[10] A.B. Spierings, N. Herres, G. Levy, Influence of the particle size distribution on surface quality and mechanical properties in AM steel parts, Rapid Prototyp. J. 17 (2011) 195–202.

[11] M. Badrossamay, E. Yasa, J. Van Vaerenbergh, J.-P. Kruth, Improving productivity rate in SLM of commercial steel powders, Tech. Pap. Manuf. Eng. (2009) 1–13.

[12] K. Abd-Elghany, D.L. Bourell, Property evaluation of 304L stainless steel fabricated by selective laser melting, Rapid Prototyp. J. 18 (2012) 420–428.

[13] B. Liu, R. Wildman, C. Tuck, I. Ashcroft, R. Hague, Investigation the Effect of Particle Size Distribution on Processing Parameters Optimisation in Selective Laser Melting Process, Addit. Manuf. Res. Group, Loughbrgh. Univ., 2011, pp. 227–238.

[14] M. Lutter-Günther, M. Horn, C. Seidel, G. Reinhart, Influence of particle size distribution on powder flowability and part properties in laser beam melting: einfluss der Korngrößenverteilung auf Fließfähigkeit und Bauteilqualität beim Laserstrahlschmelzen, Rapid. Tech—International Trade Show Conf. Addit. Manuf. Proc. 14th Rapid. Tech Conf. Erfurt, Ger. (2017) 20–22.

[15] R. Baitimerov, P. Lykov, D. Zherebtsov, L. Radionova, A. Shultc, K. Prashanth, Influence of powder characteristics on processability of AlSi12 alloy fabricated by selective laser melting, Materials (Basel) 11 (2018) 742.

[16] M. Mani, S. Feng, B. Lane, A. Donmez, S. Moylan, R. Fesperman, Measurement Science Needs for Real-Time Control of Additive Manufacturing Powder Bed Fusion Processes, US Department of Commerce, National Institute of Standards and Technology, 2015.

[17] M.D. Monzón, Z. Ortega, A. Martínez, F. Ortega, Standardization in additive manufacturing: activities carried out by international organizations and projects, Int. J. Adv. Manuf. Technol. 76 (2015) 1111–1121.

[18] S. Vock, B. Klöden, A. Kirchner, T. Weißgärber, B. Kieback, Powders for powder bed fusion: a review, Prog. Addit. Manuf. (2019) 1–15.

[19] W. Pabst, E. Gregorova, Characterization of particles and particle systems, ICT Prague 122 (2007) 122.

[20] R. Freeman, Measuring the flow properties of consolidated, conditioned and aerated powders—a comparative study using a powder rheometer and a rotational shear cell, Powder Technol. 174 (2007) 25–33.

[21] R. Freeman, X. Fu, Characterisation of powder bulk, dynamic flow and shear properties in relation to die filling, Powder Metall. 51 (2008) 196–201.

[22] S. Kolossov, E. Boillat, R. Glardon, P. Fischer, M. Locher, 3D FE simulation for temperature evolution in the selective laser sintering process, Int. J. Mach. Tools Manuf. 44 (2004) 117–123.

[23] A.V. Gusarov, I. Yadroitsev, P. Bertrand, I. Smurov, Model of radiation and heat transfer in laser-powder interaction zone at selective laser melting, J. Heat Transfer 131 (2009) 72101.

[24] R.B. Patil, V. Yadava, Finite element analysis of temperature distribution in single metallic powder layer during metal laser sintering, Int. J. Mach. Tools Manuf. 47 (2007) 1069–1080.

[25] M. Matsumoto, M. Shiomi, K. Osakada, F. Abe, Finite element analysis of single layer forming on metallic powder bed in rapid prototyping by selective laser processing, Int. J. Mach. Tools Manuf. 42 (2002) 61–67.

[26] G. Jacob, C.U. Brown, M.A. Donmez, The Influence of Spreading Metal Powders with Different Particle Size Distributions on the Powder Bed Density in Laser-Based Powder Bed Fusion Processes, (2018).

[27] B. Foster, E. Reutzel, A. Nassar, B. Hall, S. Brown, C. Dickman, Optical, layerwise monitoring of powder bed fusion, Solid Free. Fabr. Symp. Austin, TX, August, 2015, pp. 10–12.

[28] M.L. Vlasea, B. Lane, F. Lopez, S. Mekhontsev, A. Donmez, Development of powder bed fusion additive manufacturing test bed for enhanced real-time process control, Proc. Int. Solid Free. Fabr. Symp. (2015) 527–539.

[29] V. Urlea, V. Brailovski, Electropolishing and electropolishing-related allowances for IN625 alloy components fabricated by laser powder-bed fusion, Int. J. Adv. Manuf. Technol. 92 (2017) 4487–4499.

[30] S. Moylan, A. Cooke, K. Jurrens, J. Slotwinski, M.A. Donmez, A Review of Test Artifacts for Additive Manufacturing, Natl. Inst. Stand. Technol. (NIST), 2012 Gaithersburg, MD, Rep. No. NISTIR. 7858.

[31] J.A. Slotwinski, E.J. Garboczi, P.E. Stutzman, C.F. Ferraris, S.S. Watson, M.A. Peltz, Characterization of metal powders used for additive manufacturing, J. Res. Natl. Inst. Stand. Technol. 119 (2014) 460.

[32] H. Gu, H. Gong, J.J.S. Dilip, D. Pal, A. Hicks, H. Doak, B. Stucker, Effects of powder variation on the microstructure and tensile strength of Ti6Al4V parts fabricated by selective laser melting, Proc. 25th Annu. Int. Solid Free. Fabr. Symp. Austin, TX, USA, 2014, pp. 4–6.

[33] Z. Fan, H. Feng, Study on selective laser melting and heat treatment of Ti-6Al-4V alloy, Results Phys. 10 (2018) 660–664.

[34] J.-R. Poulin, A. Kreitcberg, P. Terriault, V. Brailovski, Long fatigue crack propagation behavior of laser powder bed-fused inconel 625 with intentionally-seeded porosity, Int. J. Fatigue 116 (2019) 634–647.

[35] M. Ruffo, C. Tuck, R. Hague, Empirical laser sintering time estimator for Duraform PA, Int. J. Prod. Res. 44 (2006) 5131–5146.